

Finite element analysis of small-scale hot compression testing

Patryk Jedrasiak, Hugh Shercliff *

Department of Engineering, University of Cambridge, Trumpington St, Cambridge, CB2 1PZ, UK

* Corresponding author: hrs@eng.cam.ac.uk (44-1223-332683)

Abstract

This paper models hot compression testing using a dilatometer in loading mode. These small-scale tests provide a high throughput at low cost, but are susceptible to inhomogeneity due to friction and temperature gradients. A novel method is presented for correcting the true stress-strain constitutive response over the full range of temperatures, strain-rates and strain. The nominal response from the tests is used to predict the offset in the stress-strain curves due to inhomogeneity, and this stress offset $\Delta\sigma$ is applied piecewise to the data, correcting the constitutive response in one iteration. A key new feature is the smoothing and fitting of the flow stress data as a function of temperature and strain-rate, at multiple discrete strains. The corrected model then provides quantitative prediction of the spatial and temporal variation in strain-rate and strain throughout the sample, needed to correlate the local deformation conditions with the microstructure and texture evolution. The study uses a detailed series of 144 hot compression tests of a Zr-Nb alloy. While this is an important wrought nuclear alloy in its own right, it also serves here as a test case for modelling the dilatometer for hot testing of high temperature alloys, particularly those with dual α - β phase microstructures (such as titanium alloys).

Keywords

Finite element analysis, process modelling, hot compression testing, upsetting, Zr alloys, Ti alloys.

1. Introduction

Laboratory hot compression testing is a common idealisation to inform modelling of forging and other thermomechanical processes, including characterisation of the constitutive response and prediction of final microstructure, texture and properties [1]. Even in simple lab tests, it can be difficult to achieve

homogeneity of temperature and strain, due to friction between workpiece and dies, and due to plastic heat dissipation and thermal losses to the dies and surroundings [2]. Hence “modelling the test” is necessary to correct for inhomogeneity. The principal test geometries are torsion, axial ‘upsetting’ (cylinder or ring), and plain strain compression, allowing the use of simple tools and workpieces and large strains. Direct heating systems, such as Gleeble machines, are faster to operate than air furnace heating [3], and offer higher performance in terms of maximum load, strain-rate, temperature and heating rate. But they are complex to operate, and can be difficult to control and instrument. The current work used small-scale cylindrical upsetting on a DIL 805 A/D/T Dilatometer (by TA instruments) in loading mode, to take advantage of the rapid sample throughput, precise strain measurement and good temperature control [4].

In ideal axial compression the sample undergoes uniform uniaxial compression and maintains its cylindrical shape, and calculating true stress σ and true strain ε from force and displacement is straightforward:

$$\sigma = \frac{F}{\pi D^2}, \quad \varepsilon = \ln \frac{H}{H_0} \quad (1)$$

where the dimensions are defined in Fig.1(a,b). In reality, inhomogeneous deformation occurs leading to ‘barrelling’ and a ‘dead metal zone’ adjacent to the platens (Fig. 1c). The relative influence of friction and temperature gradients is determined by experimental practicalities, such as the use of high temperature lubricants, the choice of die materials, pre-heating of the sample, or the ability to pre-heat the dies. Some inhomogeneity is inevitable, so a distinction needs to be made between ‘notional’ true stress-strain data, calculated using eqn. (1) assuming uniform strain, and the true constitutive response extracted by some means from the tests, allowing for inhomogeneity.

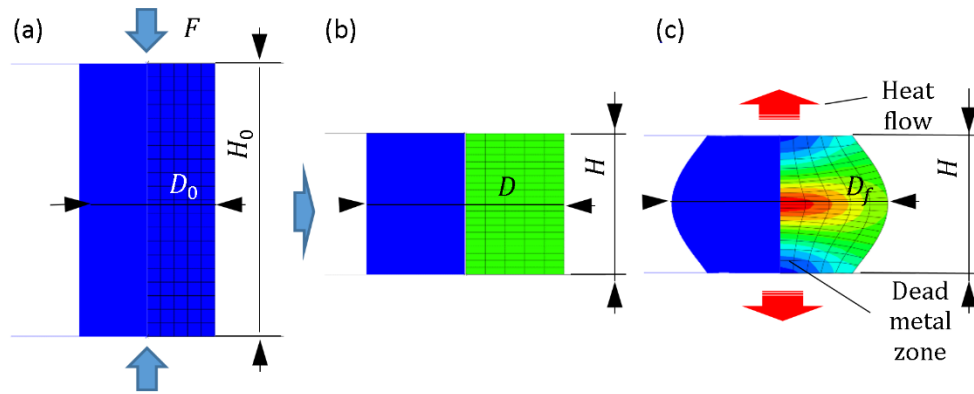


Figure 1 Cylindrical sample in uniaxial compression: (a) original dimensions; (b) ideal homogeneous compression; (c) real case, showing barrelling, due to friction and a temperature gradient.

Most authors present ‘notional’ true stress-strain curves using eqn. (1), but many fail to comment on barrelling or any compensation to account for it, potentially leaving unknown, significant uncertainty in the response. Some authors give guidance on practical limits that maintain sufficient accuracy in the evaluation of flow stress in hot upsetting, for example, Roebuck et al. [5] recommend that a barrelling coefficient B should be less than 1.1, where $B = \frac{H D_f^2}{H_0 D_0^2}$ (with dimensions as shown in Fig. 1). A minimum temperature deviation of 4°C from nominal was recommended for testing in the range 600–900°C, though at high rates (above 1s^{-1} for steels), temperature rises of 30–40°C are typical, so some compensation is required in the analysis. Hot compression tests are also often followed by correlation with microstructural evolution, which may be inaccurate if the nominal temperature, strain-rate and strain are assumed to apply throughout the sample, without taking account of spatial variations. Correction methods applied in the literature are discussed further below.

1.1 Constitutive modelling

The nature of lab testing means that constitutive data for flow stress σ are generated as continuous stress-strain curves at discrete (nominal) temperature T and strain-rate $\dot{\epsilon}$, and then fitted to some form of constitutive model $\sigma(T, \dot{\epsilon}, \epsilon)$. First principles models of flow stress seek to interpret plastic slip via dislocation mechanics in relation to internal microstructural state variables and their evolution, for

example sub-grain size, dislocation density, secondary phases and solute content [6]. Phenomenological models are calibrated to experiment using adjustable parameters, and may be based in part on underlying physical principles. Purely statistical methods such as neural networks may also be used, being well-suited to solving problems which are non-linear, provided the dataset is sufficient and the user understands how to optimise the complexity of the network and to avoid over-fitting [6]. But neural networks make no distinction between the inputs, losing the link to the underlying physics altogether – for instance, the monotonic variations of stress with temperature, strain-rate or strain are not imposed *a priori*, as in the assumed form of most empirical fits to data [1].

The Zener-Hollomon parameter $Z = \dot{\epsilon}e^{Q/RT}$ (in which R is the universal gas constant) is an established physically-based semi-empirical approach for modelling the steady-state (strain-independent) flow stress, based on a supposed quantitative equivalence between the effects of strain-rate and temperature [7]. The activation energy for diffusion Q ties the response to an underlying mechanism over given ranges of temperature and strain-rate, but the values for Q are derived empirically from the data. Sellars and Tegart [8] used the Zener-Hollomon parameter extensively to demonstrate how it correlated with hot flow stress for both hot working and creep conditions, and also with common measures of recrystallisation. The Sellars-Tegart equation has the form:

$$\dot{\epsilon} = A(\sinh \alpha\sigma)^n \exp(-Q/RT) \quad \text{or} \quad Z = A(\sinh \alpha\sigma)^n \quad (2)$$

where A , α and n are adjustable constants (though n is related to the power-law exponent for creep, falling in the range 1-8). Sellars and Tegart determined characteristic activation energies for the rate-controlling restoration process in single-phase aluminium, copper, nickel and stainless steel. More complex physically-based models are required to capture the thermally activated motion of dislocations over obstacles in two-phase materials [9] [10], while care is always needed in handling data which may lie across the transition between competing deformation mechanisms [11].

An empirical approach has been proposed for a ‘modified Sellars-Tegart equation’, in which the ‘constants’ (A , α , Q and n) are arbitrarily considered to be polynomial functions of strain. Lin et al. [12] [13] proposed such equations to fit data from hot compression tests of 42CrMo steel. This approach

introduces a very large number of adjustable parameters, with 5th order polynomials in strain for 4 parameters. Even then, the model did not provide satisfactory correlation with data, so the authors arbitrarily modified the Zener–Hollomon parameter to $Z' = \varepsilon^{4/3} e^{Q/RT}$ (changing the dimensions of Z in the process). While the fit could be improved, there is no physical justification for any of the proposed modifications. This approach has subsequently become widespread in some parts of the world, and has been applied to a number of steels [14], Al alloys [15], Mg alloys [16], Ni superalloys [17], Ti alloys [18], brass [19] and austenitic stainless steel [20]. In many cases the final quality of the fit between measured and predicted stress remains poor, with artefacts such as maxima and minima in the flow stress curves, and physically non-sensical behaviour such as curves crossing at different strain-rates. High order polynomials in strain are mathematically ill-conditioned to a parameter which ranges from 0 to typically a maximum of around 1: there will be a negligible contribution from the highest order terms (ε^4 , ε^5 , ε^6) at low strains, but these terms will dominate as strain approaches unity and above, giving very poor extrapolation. Overall therefore, in the authors' opinion, this approach is highly questionable: up to 24 adjustable parameters are statistically-fitted and cited to as many as 7 significant figures, in order to fit experimental curves which cannot themselves be replicated from test-to-test to better than a few %. Any strain-dependence of the 'constants' in the Sellars-Tegart equation must be derived from physical arguments, particularly the activation energy Q , which characterises the rate-controlling unit step of atomic diffusion in the alloy. Competing microstructural mechanisms with distinct values of Q may lead to an apparent shift in "effective" Q with temperature, strain-rate or strain (e.g. bulk diffusion versus boundary or dislocation core diffusion), but a polynomial statistical fit with strain sheds no light on the underlying metallurgical behaviour. Since this methodology turns the physically-based Sellars-Tegart equation into pure statistics, there is a strong case for dropping the use of Z altogether, and using multi-parameter statistics directly on data for $\sigma(T, \dot{\varepsilon}, \varepsilon)$, most likely in the form of a neural network. This was recognised by Ji et al. [21], who applied a neural network to data that could not be fit with a strain-compensated Sellars-Tegart equation, achieving much better results. However, it should be noted that none of these methods give reliable extrapolation outside the domain of temperature, strain-rate and strain to which the data were fitted.

The Johnson–Cook constitutive model is another well-established example of a phenomenological flow stress model incorporating strain-dependence, $\sigma(T, \dot{\varepsilon}, \varepsilon)$ [22]:

$$\sigma = (A + B\varepsilon_p^n)(1 + C \ln \frac{\dot{\varepsilon}_p}{\dot{\varepsilon}_{p0}})(1 + \left(\frac{T - T_0}{T_m - T_0}\right)^m) \quad (3)$$

where ε_p and $\dot{\varepsilon}_p$ are the equivalent plastic strain and strain-rate respectively, T_m is the melting temperature, T_0 and $\dot{\varepsilon}_{p0}$ are a reference temperature and plastic strain-rate respectively, while A, B, C, n and m are material constants – giving a total of 7 adjustable parameters. It assumes the material is isotropic, and that thermal softening, strain-hardening, and strain-rate sensitivity are three independent phenomena, i.e. the three key variables are in separate multiplicative terms. The power-law dependence on strain, and logarithmic dependence on strain-rate, have some physical justification in terms of work hardening and creep mechanisms; the temperature-dependence does not however embody the classical exponential behaviour of Arrhenius' law (i.e. $\exp - Q/RT$, with a characteristic activation energy, Q). The Johnson-Cook model (and empirical modifications thereof) is widely-used in numerical simulations, for its simplicity and the availability of fitting parameters for various materials. A modified Johnson-Cook model could in fact be fitted to the dataset from the current work, to an accuracy of +/- 10% of the maximum flow stress [23], but with limited confidence on extrapolation of the model outside the experimental domain. It is not often noted that it was originally intended for intense impulse loading and, according to the authors, is best-suited for computations where the user cannot readily incorporate more complex material models which give a more accurate description of the material behaviour [22].

1.2 Modelling of hot compression tests

Analytical models of barrelling are limited to small deformations, without taking into account strain hardening or strain-rate sensitivity. Kulkarni and Kalpakjian [24] used slip-line analysis for upsetting of an Al alloy, using multiple aspect ratios and height reductions, but concluded that a purely analytical solution for barrelling using slip-line analysis could not account for the properties of real materials. Oh et al. [25] studied the effect of an initial temperature non-uniformity in uniaxial hot compression tests of materials with contrasting temperature sensitivity of flow stress (Ti aluminide and low alloy steel).

They concluded that FEM was necessary to account for factors such as stress triaxiality, friction and heat conduction. Their model employed a constant friction shear factor m at the die-workpiece interfaces, and a fixed, linear 10°C gradient along the sample. The predicted shapes agreed well with experiments over a range of test conditions, and the influence of friction and temperature inhomogeneity on the flow stress was predicted to be less than 5%. Rao et al. [26] studied hot compression of copper with various sample geometries, with the widely-used assumptions of rigid tools and a constant friction factor m , with an isotropic plastic response characterised by the Zener-Hollomon parameter. Surface strains were measured from the distortion of a grid marked on the surface, and used to compare with predictions of the FE model.

It is common for the ‘notional’ true stress-strain data from hot compression tests to be used as an input to FE models of the same tests, as in Zhou et al. [27] for compression of M2 high speed steel, using a constant friction factor m , and neglecting heat losses. The predicted strain distribution corresponds well with the current work, with dead metal zones at the interfaces, maximum strain at the centre of the sample, and shear bands. Some authors have coupled the FE predicted strain and temperature fields with empirical relations predicting the inhomogeneous microstructure, and resulting properties – for example, Majta et al. [28] predicted the yield strength distribution in hot compression of a Nb steel.

Correction of stress-strain curves in hot compression

Stress-strain curves from hot compression tests are often corrected for friction and adiabatic heating using simple analytical formulae [29]. For example, for a coefficient of friction μ :

$$\sigma = \frac{C^2 \sigma_0}{2[\exp(C) - C - 1]} \quad (4)$$

where $C = 2\mu r/h$, σ is the corrected stress, σ_0 is the measured stress in the presence of friction; r and h are sample radius and height. Similarly, an average temperature rise due to adiabatic heating may be evaluated as:

$$\Delta T = \frac{\eta \int \sigma d\varepsilon}{\rho c} \quad (5)$$

where η is a constant adiabatic correction factor, ρ is density and c is heat capacity. A correction in flow stress for temperature can be then estimated using the Sellars-Tegart model, equation (2).

A simple upper-bound analysis of compression by Ebrahimi and Najafizadeh [30] gave an estimate of the friction factor, directly from the maximum radius and height of the deformed workpiece, without needing the load or material properties. Their method was subsequently applied by a number of authors, including Monajati et al. [29] and Li et al. [31] [32] [33]. The latter authors accounted for friction and adiabatic heating using equations (4) and (5), applied an independent analytical correction for changing strain-rate, and additionally expressed μ in hot upsetting as a function of strain, in order to extend the correction of stress-strain curves to large strains, for hypoeutectoid steel.

Analytical formulations of stress correction have also been derived from FEM results, as shown by Goetz and Semiatin [34], who used an FE model of hot upsetting to calculate the adiabatic correction factor η , i.e. the fraction of dissipated plastic heat retained in the sample after heat loss to the dies. They simulated tests at a range of strain-rates, with different die materials, and found that expressions to capture how η varied with die and sample thermal conductivities, interface heat-transfer coefficient, workpiece heat capacity, and the strain and strain-rate. Similarly, Li et al. [35] used FEM to predict the ratio of stress with and without friction, σ_z/σ , and proposed analytical formulae to compensate for the influence of friction on as-measured flow stress. Temperature effects were compensated separately using the conventional formula for adiabatic heating.

The effect of temperature change due to adiabatic heating on the stress-strain response of stainless steel, was investigated by Mataya and Sackschewsky [36], for frictionless compression. Again, the notional flow stress data at a range of nominal T and $\dot{\varepsilon}$ were used as input to the FE analysis, to calculate the instantaneous temperature at the sample centre for every test, and validated by thermocouple data. The corrected $\sigma(\varepsilon)$ curves at each nominal T and $\dot{\varepsilon}$ were then obtained by interpolation of the FE results.

Iterative correction procedures

A number of authors have proposed iterative procedures for correcting ‘notional’ true stress-strain curves for friction, using FE analysis. Parteder et al. [37] assumed isothermal conditions with sticking friction, and a rate-independent flow stress. Using each estimate of the stress-strain response as input, a dimensionless correction $c(u)$ was evaluated from the experimental and predicted force-displacement $F(u)$ curves: $c(u) = 1 - F_{test}(u)/F_{FE}(u)$. After fitting the correction $c(u)$ with a continuous function, a revised stress-strain curve was found, using $\sigma_{i+1}(\varepsilon) = \sigma_i(\varepsilon)/(1 + c(\varepsilon))$, and the process repeated until the correction was acceptably small. This highlighted the shortcomings of the simpler analytical methods for handling friction alone. A similar approach by Xinbo et al. [38] compared predicted and experimental $F(u)$ curves for two carbon steels over a range of test conditions. Here the authors sought to minimise a target error function of squared differences, $\Phi = \int (F_{exp} - F_{FEM})^2 dt$, with F_{FEM} expressed as a function of a corrected flow stress $\bar{\sigma} = f\bar{\sigma}_{exp}$, in which f is the corrective function to be applied. The analysis was repeated with each adjusted input $\bar{\sigma}$, until the target error function reduced to a pre-defined small value.

A closely-related analysis correcting for friction in hot upsetting was developed by Wang et al. [39] for a structural carbon steel and a 4×4 matrix of T and $\dot{\varepsilon}$. The friction coefficient was estimated from the sample shape, using the formula proposed in [30]. After the first run of the FE model using the notional $\sigma(\varepsilon)$ data from the experiments, the difference between experiment and FE was computed in terms of $\Delta\sigma$, that is, the predicted $F(u)$ was also converted to a notional true-stress strain response for each test. This $\Delta\sigma$ was applied to the input stress for the next run of the FE model, and the process iterated until $\Delta\sigma$ reached the required precision. Despite including heat transfer in their FE analysis, the authors did not comment on the influence of the temperature gradient or adiabatic heating in the sample.

Ring compression tests are designed to give greater precision in calibrating the friction conditions, since the change in the internal diameter D is sensitive to friction – it may increase for low levels of friction but decreases for high levels of friction. Cho and Ngalle [40] used an inverse analysis with this geometry to characterise simultaneously the frictional behaviour and flow stress, for a 6061 Al alloy. The flow

stress was assumed to take the form $\bar{\sigma} = K\bar{\varepsilon}^n$, and the analysis first optimised K and n , using a Newton-Raphson iterative method to minimise an objective function that depended on the squared differences between experimental and computed loads. The friction factor m was then optimised using the same procedure, but with a second term in the objective function dependent on the difference in predicted and measured internal diameter. This analysis also did not take into account any temperature effects.

A recent article by Yu et al. [41] used FE analysis to correct the flow stress in hot compression of Ti60 alloy on a Gleeble machine, in which it was predicted that a significant temperature gradient developed in the initially isothermal sample. Their assumed initial constitutive law was a simple separable variable function of power-laws in strain-rate and strain, and an Arrhenius temperature-dependence:

$$\sigma = A \dot{\varepsilon}^m \varepsilon^n \exp Q/RT \quad (6)$$

However, this does not follow the correct form of the Zener-Hollomon parameter in equation (2), due to the exponent on strain-rate, as evidenced by the need to use a non-physical low value of Q to compensate. The correction due to inhomogeneous deformation was then made by adding a second term that involved multiplying the measured flow stress by another function of similar form to equation (6), but with the strain term changed into a complex polynomial of four terms, with some of the exponents being non-integer adjustable parameters. Furthermore, the adjustable parameters were fitted over several discrete strain ranges, and took widely different values in each range, even changing sign. This may reflect the attempt to fit data that extended up to $\varepsilon=1.4$, where the deviation between true flow stress and measurement was predicted to be a factor of 2, and where a polynomial in strain becomes dominated by high powers of ε (as discussed in relation to other statistical fits above). At this aspect ratio however, it is likely that contact conditions in friction and pressure distribution have evolved significantly from the start of the test. So any physical basis in equation (6) and its modified form is obscured, and yet the heavily statistical fit is constrained to follow a multiplicative separable variable form of the equation in strain-rate, strain and temperature, while the final fit incorporates test data which are not available to other users. The validation is also limited to a single temperature and strain-rate, and yet the authors cite the adjustable parameters to up to six significant figures.

In summary therefore, previous correction methods share some similar features with the approach in the current work, in which the stress difference between prediction and experiment is used to update the input to the FE. Some require multiple iterations, or do not include inhomogeneous temperature, and more widely there is significant variation in the semi-empirical handling of flow stress as a function of strain-rate, strain and temperature. In the current work, both friction and a temperature gradient are incorporated, and a novel approach is used to fit both initial $\sigma(T, \dot{\epsilon}, \epsilon)$ and the final data after correction, by treating them as simple second order functions of T and $\dot{\epsilon}$ at discrete strains. Sensitivity studies of the FE model are reported in depth elsewhere [23]; the modelling methodology is summarised below, and then developed for an extensive test series on a two-phase ZrNb alloy, using a dilatometer in loading mode, in contrast to the more conventional use of a Gleeble machine.

1.3 Modelling methodology

The numerical procedure applies a systematic correction to the ‘notional’ true stress-strain curves, accounting for the influence of friction and inhomogeneous temperature. The procedure is illustrated in Figure 2, summarised as follows:

- (i) take the notional true stress-strain curves from the experiments, after suitable smoothing by fitting to second-order functions $\sigma = f(T, \dot{\epsilon})$ at discrete values of strain, and use as a lookup table for the constitutive response, $\sigma = f(T, \dot{\epsilon}, \epsilon)$ for input to the FE analysis;
- (ii) predict the force-displacement curves for the full test matrix, with suitable friction boundary conditions and non-uniform temperature field, and convert the predicted $F(u)$ curves to notional true $\sigma(\epsilon)$ curves;
- (iii) at a number of discrete strains, evaluate the *offset* in stress $\Delta\sigma = f(T, \dot{\epsilon})$ (Fig. 2a) and *subtract* $\Delta\sigma$ from the original stress-strain data used as input to the analysis, to give a corrected input dataset, which is re-fitted to second-order functions $\sigma = f(T, \dot{\epsilon})$ at discrete values of strain (Fig. 2b);
- (iv) re-run the analysis with the corrected input constitutive data, and compare the experimental and predicted notional true stress-strain curve for every test (Fig. 2c).

Friction and a temperature gradient offset the deformation conditions away from the nominal values. If the initial estimate for the constitutive data captures the strain-rate and temperature dependence of the flow stress to sufficient accuracy, then the correction of the data can be achieved in a single iteration. In this work there was a plentiful set of tests to give a robust starting point for the analysis. This is unusual in practice – more often the tests might only cover a 3×3 matrix of T and $\dot{\epsilon}$. In this case, an alternative starting point may be a constitutive response from the literature, for a similar alloy to the test case, in order to find $\Delta\sigma = f(T, \dot{\epsilon}, \epsilon)$. An example of this approach is under investigation for a series of hot compression tests on two Ti alloys, using the same dilatometer rig [42].

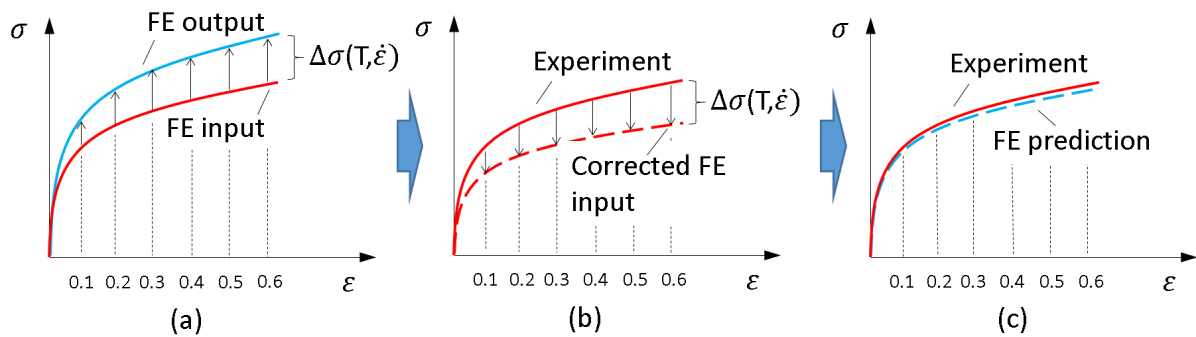


Figure 2 Methodology for correcting true stress-strain response: (a) Calculating correction $\Delta\sigma = f(T, \dot{\epsilon}, \epsilon)$ from initial $\sigma = f(T, \dot{\epsilon}, \epsilon)$ input to the FE and the predicted $\sigma(\epsilon)$; (b) applying correction $\Delta\sigma = f(T, \dot{\epsilon}, \epsilon)$ to the initial $\sigma = f(T, \dot{\epsilon}, \epsilon)$; (c) validation of corrected constitutive data.

2. *Experimental Work*

The dilatometer data was obtained from experiments conducted by collaborators at Manchester University, and is presented in detail elsewhere [43] [44]. The material was an industrial Zr-2.5Nb alloy, the alternative to Zr-Sn zircalloys used for cladding and pressurised tubing in nuclear reactors. Zr-2.5Nb is a two-phase material of hexagonal close-packed α and body-centred cubic β phases. The alloy in this study was processed to obtain a microstructure of Widmanstätten packets of α -laths, separated by fine-scale retained metastable β [43]. Cylindrical samples of diameter 5mm and length 10mm were machined with the cylinder axis parallel to the prior rolling direction.

The test conditions covered a 9×8 matrix, with temperatures from 650–850°C in 25°C intervals, strain-rates from $10^{-2.5}$ – 10 s⁻¹, in intervals of $10^{0.5}$ s⁻¹, and a maximum true strain in all cases of 0.7. The entire matrix of 72 tests was duplicated to investigate machine repeatability and sample-to-sample variability due to microstructural variation. Hot compression testing was performed using a TA Instruments DIL 805 A/D/T Dilatometer in loading mode, which potentially offers better temperature and strain-rate control compared to alternative testing machines (e.g. Gleeble 3500). The sample sits under vacuum between Si₃N₄ platens, inside a copper induction coil for heating, and is cooled using He gas. The experiments were displacement-controlled, varying the platen velocity to maintain the target true strain-rate as the sample length decreases, measured by LVDT transducer. The DIL 805 takes up to 11,000 readings throughout the deformation phase, with a logging frequency up to 500Hz. The temperature was monitored by an S-type thermocouple, with an accuracy of $\pm 1.5^\circ\text{C}$ or $\pm 0.25\%$, spot welded to the surface at the mid-plane. At the higher strain-rates, $10^{0.5}$ s⁻¹ and 10 s⁻¹, a graphite lubricant was applied to both ends of the sample. The maximum true strain in each test was 0.7.

Significant barrelling was observed in all cases (Fig. 3), with a varying degree of asymmetrical deformation, caused by the relatively large size of the prior β grains compared to the sample size, with only three or four grains across the sample diameter. This sets a practical limit on the precision that should be sought in numerical modelling of the tests using isotropic plasticity, which can be considered to represent an average deformation response for the material.

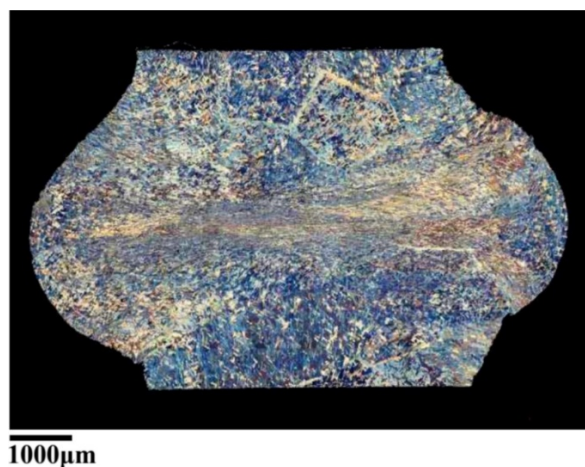


Figure 3 Microstructure and barrelling of a Zr-2.5Nb sample deformed with a nominal temperature of 800°C and strain-rate of 0.0032 s⁻¹ [44].

The thermocouple data show that the dilatometer maintained the test temperature at low strain-rates (Fig. 4a), but at the highest strain-rates, the temperature increased by 20–60°C early in the hot compression stage (Fig. 4b). This was caused by plastic dissipation at rates that were too rapid to be compensated by the He gas cooling system and radial thermal conduction. In subsequent work on Ti alloys with broadly comparable flow stress and thermal properties [42] it was also observed that cooling by the platens reduced the temperature near the platens by 40–80°C below the nominal temperature. The combination of heating due to plastic dissipation, and cooling by the platens, can therefore lead to a significant temperature gradient of order 50–100°C. The model presented in this paper investigates the effect of the temperature gradient by assuming a fixed temperature distribution. Modelling the full thermal field throughout the test is reported in subsequent work on Ti [42], in which multiple thermocouples were used.

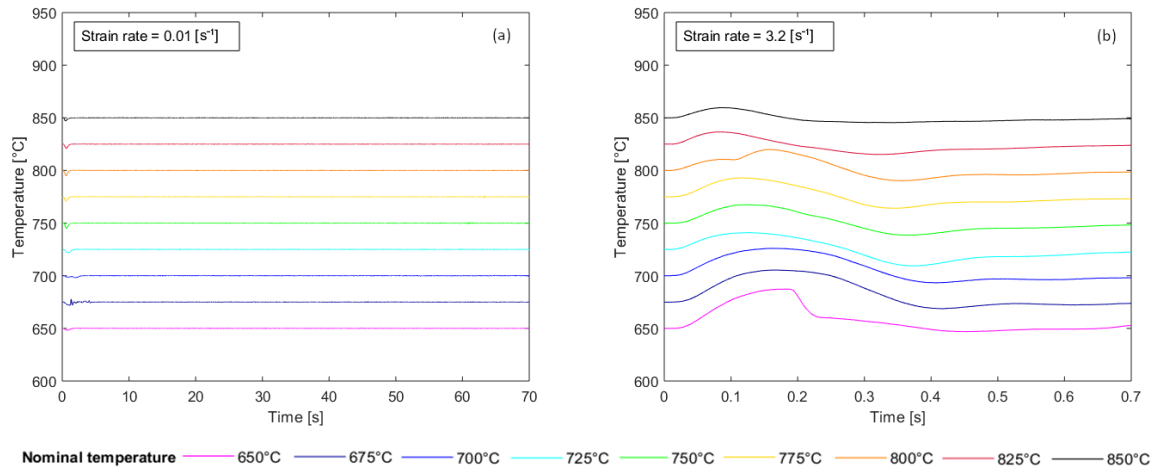


Figure 4 Thermocouple data for the hot compression stage at selected nominal $\dot{\epsilon}$ and T conditions.

“Notional” true stress-strain curves were obtained from force-displacement $F(\delta)$ data using equation (1), i.e. assuming homogenous deformation. Figure 5 shows representative curves at a low and a high strain-rate, for all test temperatures (solid lines – the dashed lines show curve-fits that are discussed later). Most pairs of repeat $F(\delta)$ curves showed minimal scatter and good repeatability. Of 144 raw

datasets, 31 unreliable curves were rejected, where two duplicate tests were significantly different (usually at high strain-rates), or the curves showed anomalous spikes or offsets. Figure 5 shows that at high strain-rate the apparent elastic-plastic transition was spread over a much greater strain (up to $\varepsilon = 0.03$), compared to the clearer elastic-plastic yield point seen at low strain-rate. This highlights the limits in the capacity of the dilatometer at these stresses and strain-rates, with the shape of the curves becoming unreliable. The data for the top two strain-rates were therefore excluded from the analysis.

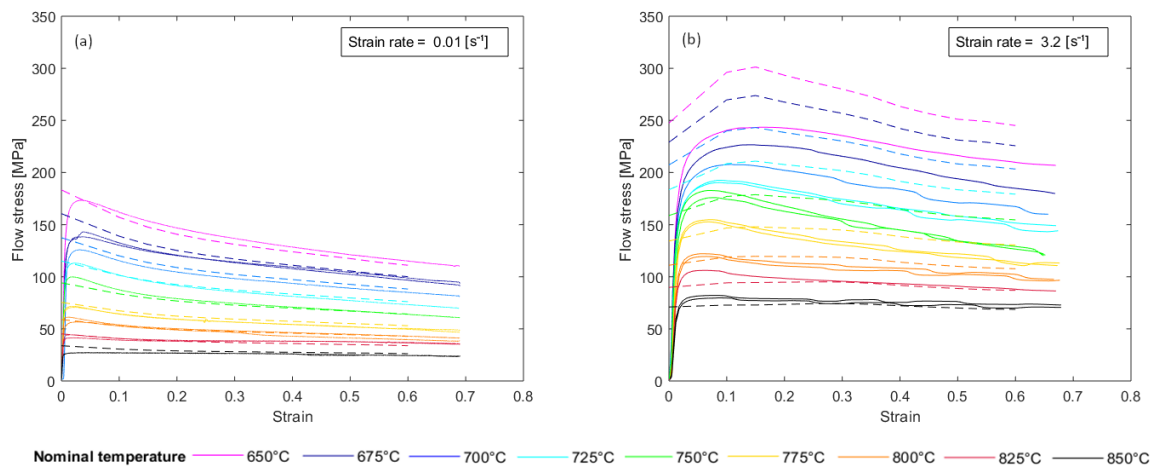


Figure 5 Notional true stress-strain curves for Zr-2.5Nb calculated directly from experimental data (solid lines), and the smoothed data fit (dashed lines), at selected nominal $\dot{\varepsilon}$ and T conditions.

To generate a lookup table for flow stress $\sigma = f(T, \dot{\varepsilon}, \varepsilon)$, and to explore different model fitting processes, an unconventional approach was adopted. The nature of testing means that continuous $\sigma(\varepsilon)$ curves are measured at discrete temperatures and strain-rates, and this perhaps leads to an inherent bias towards regarding the data as continuous in strain, but discrete in temperature and strain-rate. But physically this is a multi-dimensional function, $\sigma = f(T, \dot{\varepsilon}, \varepsilon)$, and the variation in stress is far greater with T and $\dot{\varepsilon}$ than with strain (as in Fig. 5). So it is equally valid to explore the variation in the data with respect to temperature and strain-rate at constant values of strain. The curves were therefore discretized at strain intervals of 0.05, with the two flow stress values from repeat tests being averaged

at each temperature and strain-rate (unless one curve had been rejected, in which case the single value was retained).

3. *Material constitutive data modelling*

As outlined in section 1, the correction method requires a first estimate of the flow stress $\sigma = f(T, \dot{\epsilon}, \epsilon)$ as input to the FE analysis, either as a look-up table or a smooth best-fit function. A number of fits to the raw stress-strain data were considered in [23], e.g. the Johnson-Cook model, or Sellars-Tegart model. Using a function as input is faster than interpolating from a look-up table, so best-fit functions were used for setting up the FE model (e.g. for checks on convergence and mesh size, and sensitivity analysis on the effects of friction and temperature gradient). However, curve-fitting risks losing accuracy in the original data, so for the full analysis of the correction to flow stress, it was preferable to revert to a "look-up table" for flow stress $\sigma = f(T, \dot{\epsilon}, \epsilon)$, using data from the "notional" true stress-strain curves directly, with some judicious smoothing.

The raw data in Fig. 6 show that the flow stress at a given strain-rate does not fall smoothly with increasing temperature (solid lines – the dashed lines show curve-fits that are discussed below). Similarly, at constant temperature the gradient of flow stress with strain-rate should be positive everywhere, but point-to-point values give negative strain-rate sensitivity – in particular, at high strain-rates and lower temperatures. Extrapolating the flow stress beyond the test matrix exacerbates these problems, leading to convergence issues in the FE analysis. Data smoothing was therefore required to avoid non-physical artefacts, while retaining accuracy. A common practice is to fit a model statistically using adjustable parameters to give smooth functions, eliminating the scatter highlighted above, and enabling more robust extrapolation. Sample smoothing methods are presented below, with more extensive analysis in [23].

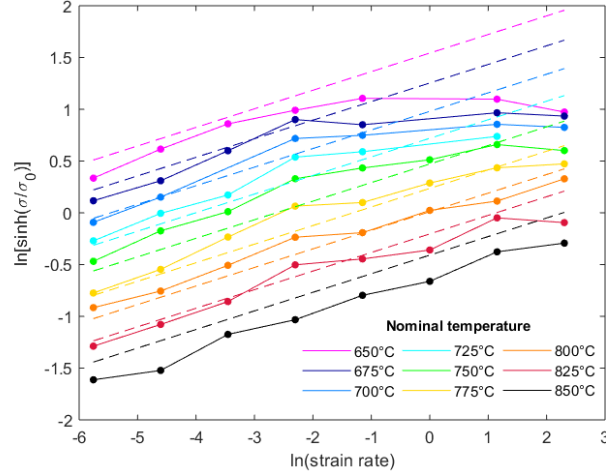


Figure 6 Experimental notional true stress of Zr2.5Nb (solid lines) at a strain of 0.05, with the best fit to the Sellars-Tegart equation (dashed lines).

The material model assumes isotropic plasticity, in spite of the strong texture in Zr-2.5Nb, in order to account for the first-order effects of inhomogeneous deformation and barrelling. More detailed simulations (such as crystal plasticity FE) could then be applied using more accurate local deformation conditions, rather than simply assuming the nominal test temperature and strain-rate apply. Other material properties in the analysis, i.e. density, Young's modulus and Poisson's ratio, were specified as independent of temperature [45] [46], as the elastic deformation is very small. Thermal properties (thermal conductivity and specific heat) are not needed in this model, since a constant temperature distribution is imposed throughout the entire test, as a first-order approximation.

3.1 Sellars-Tegart model: statistical fitting to flow stress data at low strain

A Sellars-Tegart model was investigated for $\sigma = f(T, \dot{\epsilon})$ at a low value of plastic strain, neglecting subsequent hardening or softening. To facilitate the analysis, equation (2) was re-expressed in a dimensionally homogeneous form, substituting $\dot{\epsilon}_0 = A$, and $\sigma_0 = \frac{1}{\alpha}$:

$$\frac{\dot{\epsilon}}{\dot{\epsilon}_0} = \left(\sinh \frac{\sigma}{\sigma_0} \right)^n \exp \left(-\frac{Q}{RT} \right) \quad (7)$$

This form of the Sellars-Tegart equation was fitted to $\sigma(T, \dot{\epsilon})$ data at a strain $\epsilon=0.05$ (as the data did not have sufficient reliability near the yield strain of order 0.2%), with the top two strain-rates excluded (as discussed previously). To facilitate linear regression, equation (7) was written in the following form:

$$\ln\left[\sinh\left(\frac{\sigma}{\sigma_0}\right)\right] = -\frac{1}{n} \ln \dot{\epsilon}_0 + \frac{1}{n} \ln \dot{\epsilon} + \frac{Q}{nR} \left(\frac{1}{T}\right) \quad (8)$$

This is then a linear function of the form:

$$y = \theta_0 + \theta_1 x_1 + \theta_2 x_2 \quad (9)$$

where $y = \ln\left[\sinh\left(\frac{\sigma}{\sigma_0}\right)\right]$ is the dependent variable, and $x_1 = \ln \dot{\epsilon}$ and $x_2 = \frac{1}{T}$ are the independent variables; the adjustable coefficients of the linear function are: $\theta_0 = -\frac{1}{n} \ln \dot{\epsilon}_0$, $\theta_1 = \frac{1}{n}$ and $\theta_2 = \frac{Q}{nR}$.

A least squares analysis of the experimental data at a given strain was obtained by multi-variable linear regression. The value of σ_0 had to be adjusted independently – multiple trial values were used for each analysis, in order to evaluate y , and the value chosen was that which minimised the cost function. Figure 6 shows the best-fit Sellars-Tegart model superimposed on the raw data, using axes that reflect the form of equation (8). The prediction of the high strain-rate data is included, even though these data were excluded from the analysis. The predicted flow stress is much higher than measured at low temperatures, providing circumstantial evidence that the high $\dot{\epsilon}$ / low T data are not reliable.

The best fit values of the activation energy Q and constants $\dot{\epsilon}_0$, σ_0 and n are listed in Table 1. The two most physically constrained parameters are Q and n . The value of σ_0 has some physical relevance as this value determines where on the *sinh* function the data are located – the range of $\left(\frac{\sigma}{\sigma_0}\right)$ is of the order 0.2–1.5 in this case. Experimental determination and modelling of diffusion rates in β -Zr-Nb alloys were discussed in [47], in the temperature range above 750°C. The data suggest a conventional one-defect diffusion mechanism operates, though the authors note that conventional Arrhenius plots of diffusion rate D against $1/T$ show anomalous curvature, and cite governing activation energies of order 320–370 kJ/mol. Indicative values of self-diffusion activation energy may be estimated from the melting point, using $Q \approx 0.0015 T_m$ [47], giving a value of 319 kJ/mol. This correlation is evident in

the range of values from 126 and 416 kJ/mol determined by Sellars and Tegart [8], for alloys of aluminium, copper, nickel and stainless steel. So an activation energy Q of order 450 kJ/mol is rather high, and can only realistically be regarded as an empirical fitting parameter. The accuracy of the fitted Sellars-Tegart model was better than $\pm 10\%$ σ_{max} , but the questionable value of Q means that this approach does not provide any physical insight about the underlying mechanisms.

Q_{avg} [kJ/mol]	σ_0 [MPa]	n	$\dot{\epsilon}_0$ [s ⁻¹]
469	125	5.6	6.21×10^{22}

Table 1 Best-fit parameter values for the Sellars-Tegart equation (6), fitted to experimental $\sigma(T, \dot{\epsilon})$ data for $\epsilon = 0.05$.

This perfectly plastic fit to the Sellars-Tegart equation was deemed sufficient for building a first model of the dilatometer experiments, for sensitivity analysis and optimisation of the mesh size [23].

3.2 Constitutive response: smoothing raw experimental data

For the complete analysis of barrelling due to friction and a temperature gradient, and correction of the true stress-strain response, a lookup table is required for the constitutive response $\sigma = f(T, \dot{\epsilon}, \epsilon)$, as no suitable model could be fitted to the data [23]. Given the scatter evident in Fig. 6, a smoothing process was needed to overcome non-physical artefacts, such as local negative strain-rate sensitivity, while avoiding loss of accuracy and the introduction of artificial fluctuations in individual stress-strain curves. It is also important for the purposes of numerical stability in FE analysis, where local non-physical variation with temperature or strain-rate may cause convergence problems.

It is common to achieve smoothing by curve-fitting each dataset at either fixed temperature or strain-rate, for example, by fitting multiple 1st or 2nd order polynomials to $\sigma = f(\log \dot{\epsilon})$, at constant strain and nominal temperature. While this may eliminate artificial turning points and negative strain-rate sensitivity, it takes no account of the systematic and equally physical variation with temperature. A better way to smooth with respect to both temperature *and* strain-rate is therefore to apply a low order

surface fit to $\log \sigma = f(T, \log \dot{\epsilon})$ data at each value of strain, and to check that the resulting $\sigma(\epsilon)$ curves retain their smooth shape (i.e. with a continuous hardening response, or with a single maximum followed by softening). Note that this approach avoids the over-constraint of assuming a separable variable multiplicative function of $\sigma = f(T, \dot{\epsilon}, \epsilon)$, which has led to complex modifications of physical ‘constants’ and large numbers of adjustable parameters, as discussed in the Introduction.

A planar surface fit was unable to capture the curvature of $\log \sigma$ with respect to T and $\log \dot{\epsilon}$. A second order surface fit was therefore trialled to give the simplest functional form possible, balanced in its dependence on these two variables:

$$\log(\sigma) = c_0 + c_1 T + c_2 \log(\dot{\epsilon}) + c_3 T \log(\dot{\epsilon}) + c_4 T^2 + c_5 (\log(\dot{\epsilon}))^2 \quad (10)$$

where c_1, c_2, c_3, c_4 and c_5 are constants. Note that the use of $\log(\sigma)$ and $\log(\dot{\epsilon})$ more closely linearises the problem. Equation (10) was fitted to the clean dataset (with outlier and high strain-rate curves excluded) at discrete strains from 0.05 to 0.6, in intervals of 0.05. Figure 7 shows projected views of the resulting surface fit for $\epsilon = 0.05$, viewed along the strain-rate and temperature axes in turn.

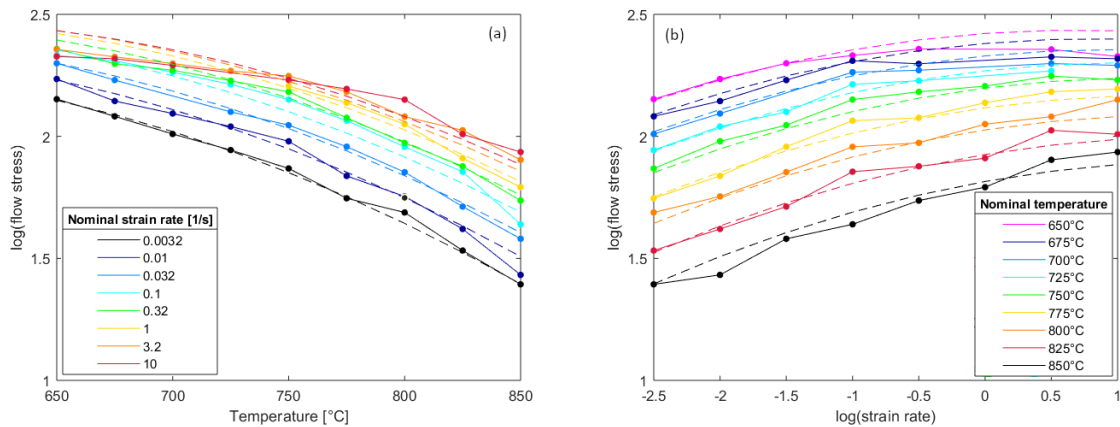


Figure 7 Projected views of a second order surface fit to $\log \sigma = f(T, \log (\dot{\epsilon}))$ (dashed lines), compared with experimental notional true stress of Zr2.5Nb (solid lines) at $\epsilon = 0.05$.

Note that the slope of the fitted curves with respect to temperature is negative everywhere (Fig. 7a), and with respect to strain-rate is positive everywhere (Fig. 7b), with no discrete curves crossing one another.

The agreement with the excluded high $\dot{\epsilon}$ / low T data is again poor, as expected. A closer fit to the data could doubtless be achieved using a higher order function with more adjustable parameters, but this is more likely to introduce artificial turning points and unstable extrapolation. Overall, the quality of the procedure was good, with individual datapoints adjusted by less than 10% σ_{max} .

The first strain value used in the fit is $\epsilon=0.05$, but for FE analysis the data must start from zero strain. It was noted earlier that it is difficult to capture the elastic-plastic transition accurately with the dilatometer, particularly at higher strain-rates. The elastic contribution to strain is negligibly small, but it remains necessary to manage the elastic-plastic transition in a numerically stable and physically realistic way. For the Sellars-Tegart model there is no strain-dependence, so a constant flow stress was simply applied from zero strain. However, the smoothed data is strain-dependent. To handle this, the flow stress values from the first two datapoints in the lookup table (at each temperature and strain-rate) were extrapolated linearly to zero plastic strain, and added to the lookup table. The complete stress-strain curves are superimposed in Fig. 5, confirming that the smoothed model curves remain smooth. Since the smoothing process produces a different surface function $\log \sigma = f(T, \log \dot{\epsilon})$ at each discrete strain, it is not in a form suitable for implementation in the FE analysis. The data were therefore input as a look-up table at discrete values of all three variables, $\sigma(T, \dot{\epsilon}, \epsilon)$, providing a numerically robust starting dataset that is close to the raw data, for the computation of the correction due to friction and inhomogeneous temperature.

3.3 Extrapolation of the constitutive response

A final issue that becomes evident in the FE analysis below is that of extrapolation of the flow stress response beyond the domain of the experimental data. Due to the temperature gradient in the sample, the minimum temperature in the analysis extends below the lowest test temperature of 650°C. And in practice adiabatic heating at high strain-rate extends the maximum temperature above the highest nominal test temperature of 850°C. Furthermore, the presence of friction and a temperature gradient generates a “dead metal zone” (DMZ) under the platens (see Fig. 1). As a consequence, the maximum local strain-rate and strain in the sample centre prove to be roughly 3 times greater than the nominal

value, while the strain-rate and strain both fall to zero in the DMZ. Extrapolation of the constitutive law must therefore cover this wider domain of conditions, and care must be taken to avoid generating artefacts in flow stress. It is well-established for all metallic systems that the dominant deformation mechanism changes as temperature and strain-rate vary – commonly presented as “deformation mechanism maps” [11]. At constant temperature, decreasing the strain-rate commonly leads to a transition from dislocation-controlled behavior (at the strain-rates characteristic of hot forming) to diffusion-controlled creep.

This is a generic issue in modelling of forging operations, which all produce a degree of inhomogeneity in the strain-rate, and will commonly include zero or very low strain regions – due to constrained contact with the tooling, or shape complexity in the part, or the incremental repetitive nature of the process (as in cogging for example). On the timescale of hot working, the strains in low strain-rate regions are negligibly small. So it may be assumed that the transition region from zero strain-rate to hot working strain-rates is narrow, and so the effect of this extrapolation can be neglected, but nonetheless the FE model must still operate smoothly down to zero strain-rate.

Figure 8 shows the fitted flow stress model for strain = 0.05, and the raw experimental data, extrapolated downwards to 600°C and to a strain-rate of $10^{-4.5} \text{ s}^{-1}$. The loss of fit in the regime of high strain-rates and low temperatures is again apparent, as discussed previously. Note that by smoothing using $\log(\sigma)$ and $\log(\dot{\epsilon})$ the extrapolation avoids artefacts such as a negative flow stress (as is also automatically achieved with the Sellars-Tegart equation), so the quadratic form of equation (10) also provides the numerical rigour needed to manage the transition into the dead metal zone. For numerical simplicity, the flow stress was assumed to be quasi-static, and unchanging with strain-rate below its value at 10^{-4} s^{-1} . Similarly, some curves extrapolated to high strain-rates reached a broad maximum, so the curves were assumed to be rate-independent above this value. Figure 6 showed that the stress-strain curves have low slopes at large strain. Hence above the final value of strain in the lookup table the response was assumed to be perfectly plastic.

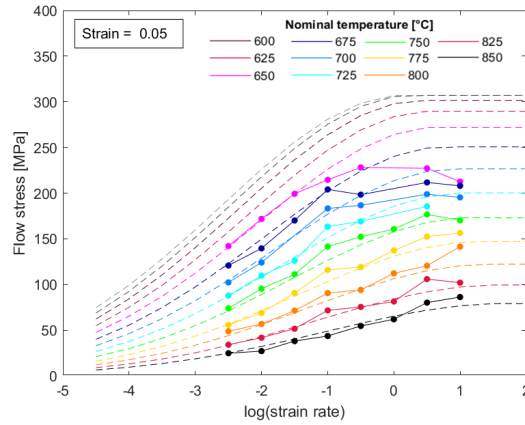


Figure 8 Flow stress vs. $\log(\text{strain-rate})$ experimental data (for strain = 0.05), and the fitted model (dashed lines) extrapolated to lower temperatures and strain-rates.

4. Finite Element Model

4.1 FE model: geometry and mesh

The cylindrical geometry of the sample allowed a computationally efficient, axisymmetric finite element model to be used, as shown in Fig. 9, with the initial length and radius shown. As the model does not include heat transfer or deformation of the platens, these were simplified to rigid bodies. The FE model used ABAQUS 2018.

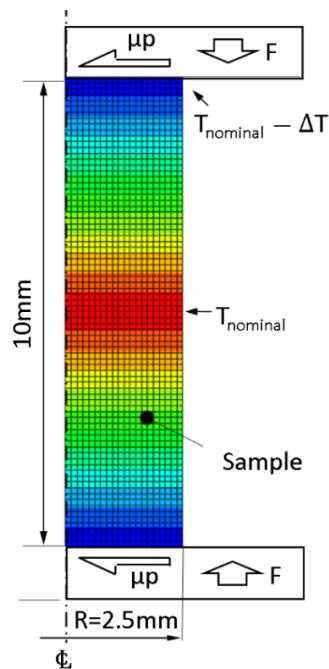


Figure 9 Axisymmetric finite element model of the hot compression dilatometer workpiece:
undeformed geometry, mesh and boundary conditions

The optimum mesh size was established in a sensitivity analysis [23], with the number of elements ranging from 400 to 25600. A mesh size of 0.125mm in the length and radial directions, corresponding to 1600 elements (as in Fig. 9), was found to give the best compromise between accuracy and computational time. Four-node thermally coupled axisymmetric quadrilateral, bilinear displacement and temperature elements were used, with enhanced hourglass control.

4.2 FE model: temperature distribution

The temperature gradient reflects both heat losses to the platens, and plastic dissipation, which will be concentrated towards the mid-section of the samples (due to the dead metal zone). In the current work, in the absence of temperature data from instrumented tests, a fixed temperature difference ΔT was maintained, from the nominal test temperature at the centre of the sample to a specified temperature difference ΔT below nominal at the platen interface (Fig. 9). The maximum temperature gradient recorded experimentally in hot compression of Ti alloys was $\Delta T = 100^\circ\text{C}$, under similar conditions on the same dilatometer instrumented with multiple thermocouples along the sample, and noting that the thermal properties are reasonably similar in ZrNb and Ti alloys. In reality, the temperature differential along the sample axis does not remain constant as assumed here, but will tend to decrease throughout the test, as the sample shortens. A differential temperature $\Delta T = 100^\circ\text{C}$ therefore represents a ‘worst case’ upper bound, while the isothermal case is a lower bound. The temperature at every node was maintained constant throughout the analysis, so the local gradient evolves as the sample deforms.

4.3 FE model: frictional boundary conditions

Frictional stresses at the interface are complex, dependent on the materials, temperature, roughness and other factors, beyond the scope of any experimental validation. As a practical approximation, Coulomb friction was specified at the interfaces between the sample and platens (Fig. 9), with the friction coefficient treated as an adjustable, average parameter. Multiple cases were used in the sensitivity

studies [23], ranging from frictionless ($\mu = 0$) to no slip at the interface (represented effectively by a coefficient of friction $\mu = 0.5$, for which the radial spread at the platen was negligible). Note that in every variant of the analysis, a sanity check was always conducted on the FE model, by analysing the frictionless case ($\mu=0$) with homogeneous temperature ($\Delta T=0$), to confirm that the predicted output true stress-strain response matched the input exactly, as expected.

The high friction no-slip condition led to convergence problems with the preferred implicit time integration, due to significant mesh distortion at the edge of the contact. The convergence problems were solved across all test conditions using a contact relationship in which the contact pressure was a user-defined piecewise linear function of the clearance between the surfaces. As a result of the problems with handling friction, and also as a consequence of the mesh distortion, the distribution of stresses at the platen interface proved somewhat unreliable. At large strains, the radial distribution of pressure $p(r)$ at the platen-workpiece interface showed a pressure spike close to the edge. However, it may be noted that: (a) the stresses at the platen are mostly below yield (giving a dead metal zone); and (b) the mid-section of the sample is fully yielding, and the conditions here therefore determine the net force at a given displacement. The pressure distribution at the platen is thus constrained to be in equilibrium with the correct net load, even if the detail of the radial variation is uncertain. So while the $p(r)$ variation is unreliable, this does not influence the accuracy of the prediction of the net force or the correction of the constitutive response, nor does it influence the prediction of deformation conditions in the plastic zone around the mid-section, which is the region of interest for microstructural studies.

5. FE modelling: sensitivity studies

The FE model was first used for sensitivity analysis into the effect of friction coefficient and temperature gradient for different combinations of nominal temperature and strain-rate, and to optimize the mesh size. Comparisons were made between predicted force-displacement responses, and between “notional” true stress-strain responses (i.e. only accounting for length and average area, not inhomogeneity), as well as the barrelled shape, and the spatial distribution of stress, strain and strain-rate within the workpiece. A standard ‘worst case’ was used as a reference, with friction coefficient μ

$\mu = 0.5$, and temperature difference $\Delta T = 100^\circ\text{C}$, mostly focussed on mid-range test conditions, $T = 750^\circ\text{C}$ and $\dot{\epsilon} = 0.1 \text{ s}^{-1}$. The isothermal, frictionless case provided a benchmark for quantifying the scale of the influence of friction and temperature gradient on the force-displacement response. These studies used the perfectly plastic Sellars-Tegart model for initial computational efficiency, and then switched to the smoothed raw data (as in Fig. 8) for detailed comparisons; full results are reported elsewhere [23]. Sample results are shown in Fig. 10 for 4 combinations of friction coefficient and temperature gradient, illustrating that the temperature gradient leads to a much stronger increase in the axial force than does the friction coefficient.

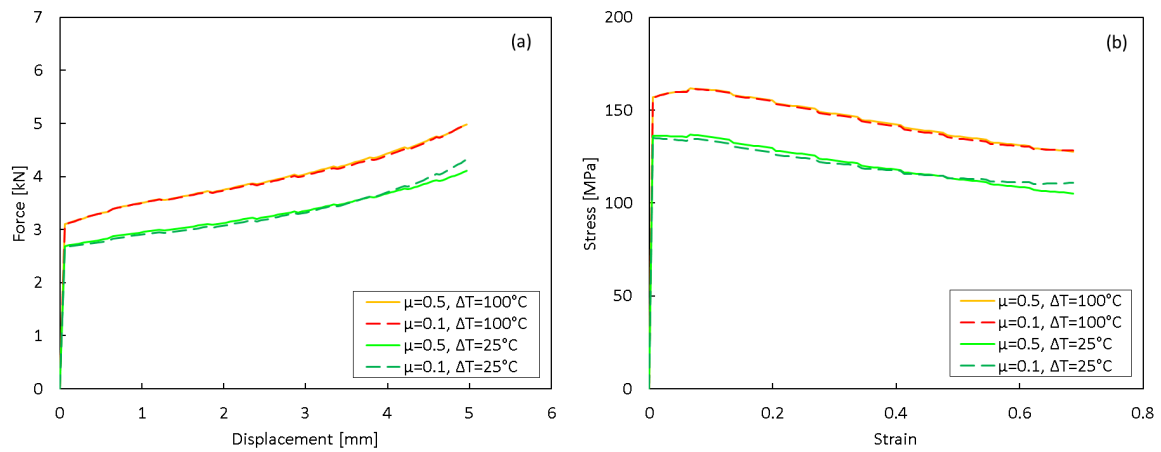


Figure 10 Predictions of the FE model using smoothed stress-strain data as input, at $T_{\text{nominal}} = 750^\circ\text{C}$, $\dot{\epsilon}_{\text{nominal}} = 0.1 \text{ s}^{-1}$, for selected combinations of friction coefficient and temperature gradient:

(a) force vs. displacement; (b) “notional” true stress vs. strain.

Further observations from the sensitivity analyses are:

- both friction and a temperature gradient lead to significant dead metal zones and barrelling, with temperature gradient having a more prominent role than friction;
- friction alone leads to barrelling with convex curvature; in contrast, a temperature gradient acting alone leads to a distinct concave/convex barrellled shape with a point of inflection, closely resembling the cross-section observed experimentally (Fig. 3);
- the strain and strain-rate across the mid-section of the sample is inhomogeneous, with peak values around 3–4 times the nominal test values;

- the notional true stress-strain response inferred directly from the load-displacement curves is substantially different from the material response used as input, so a correction must be applied.

6. Constitutive response – correction method

The FE model was used to apply a systematic correction to the true stress-strain response, to account for the influence of friction and inhomogeneous temperature. For this analysis, the boundary conditions were chosen to be a friction coefficient $\mu = 0.5$ and a fixed temperature gradient $\Delta T = 50^\circ\text{C}$. This was selected as a mid-range representative value, rather than the upper bound value of 100°C used in building and testing the model. It also reflected further experimental results on Ti alloys using the same dilatometer [42]. Note that as the actual temperature gradient in each test is unknown in the ZrNb experiments, it is not claimed that the “corrected” stress-strain data and predictions of deformation histories are accurate, but should only be regarded as a proof of concept.

The correction procedure is summarised in Fig. 2 for a single set of nominal test conditions. Starting from the smoothed and extrapolated experimental data as the input to the FE, the offset in the stress-strain curve $\Delta\sigma(\varepsilon)$ was predicted by the FE model, for all 72 combinations of T and $\dot{\varepsilon}$. Figure 11 shows sample curves for a 2×2 matrix of test conditions. The offset in stress $\Delta\sigma$ was extracted at discrete strain intervals of 0.05 up to $\varepsilon=0.7$, and plotted as a function of T and $\dot{\varepsilon}$ at each strain. Figure 12 shows the results for strains of 0.05 and 0.5. Note that the correction $\Delta\sigma$ shows a peak as temperature varies, though rises monotonically with increasing strain-rate (excepting the low T / high $\dot{\varepsilon}$ conditions).

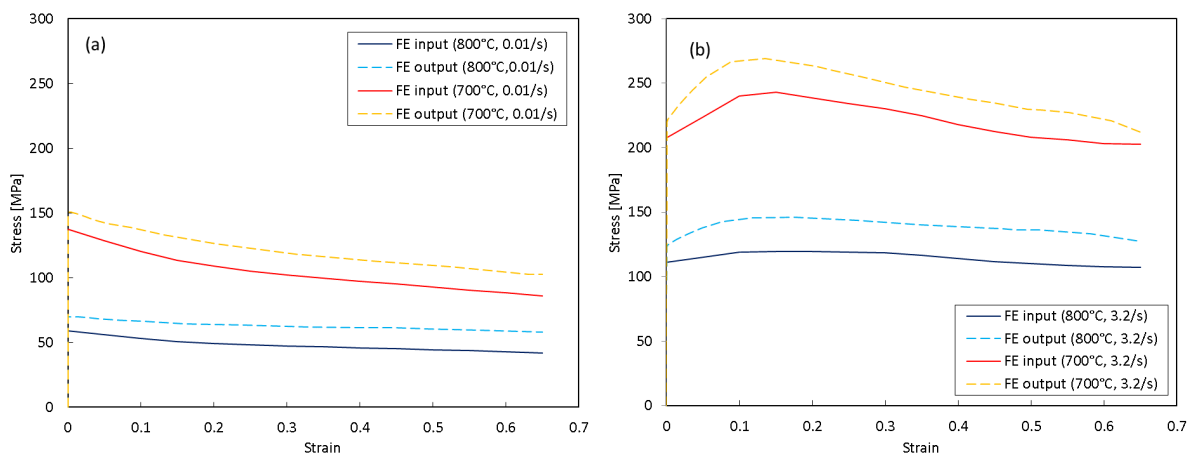


Figure 11 Stress-strain curves used as input to the FE analysis (solid curves) vs. FE predicted output (dashed curves), for nominal temperatures of 700 and 800°C and strain-rates of: (a) 0.01s⁻¹; (b) 3.2s⁻¹.

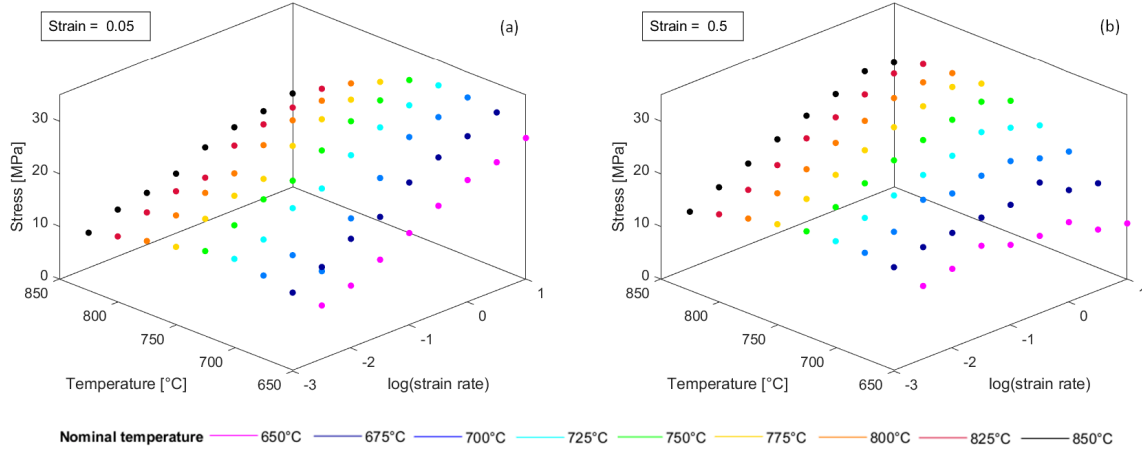


Figure 12 Stress correction $\Delta\sigma$ for all experimental combinations of temperature T and $\log(\text{strain rate}, \dot{\epsilon})$, for strains of: (a) $\epsilon=0.05$; (b) $\epsilon=0.5$.

The curvature of the correction surface $\Delta\sigma = f(T, \dot{\epsilon})$ is apparent in Fig. 12. A first iteration of the model attempted to fit the data to a surface function, using a greatly reduced dataset consisting of the 2×2 matrix of tests shown in Fig. 11. But with only four points, the function was approximated to a planar surface, giving very poor extrapolation to the peripheral test conditions – and in some cases a correction that exceeded the original flow stress. It was therefore necessary to use the correction at all 72 nominal test conditions (as in Fig 12), and to subtract this correction $\Delta\sigma = f(T, \dot{\epsilon})$ from the input data point-by-point, at each discrete strain. Equation (10) was then re-fitted to the corrected data to give a smoothed constitutive law, $\log \sigma = f(T, \log \dot{\epsilon})$, for strains up to 0.7, in intervals of 0.05 – sample stress-strain curves are shown in Fig. 13. The corrected functions were converted to a look-up table for implementation in the FE model.

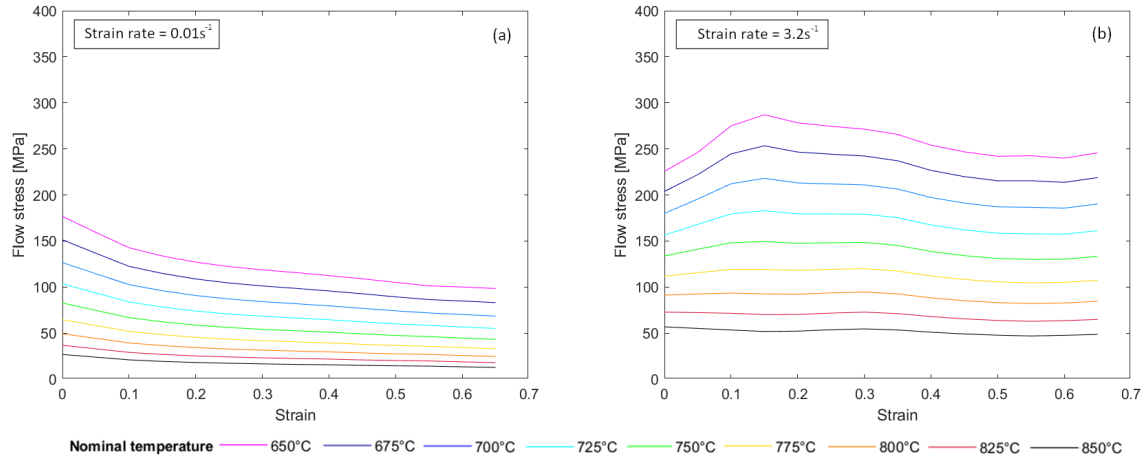


Figure 13 Corrected stress-strain curves for selected nominal test conditions.

To validate the corrected constitutive data, the experimental data were re-predicted using the model – Fig. 14 shows the results for the same 2×2 matrix of tests as in Fig. 11. The fit between prediction and experiment is good, and this was the case over most of the complete 9×8 matrix of test conditions, with the exception of the higher strain-rate tests. This is not surprising, when these tests were excluded from the original fitting of the raw data (due to adiabatic heating), and the predicted correction in stress was also anomalous in this domain.

In summary therefore, the correction method proves robust, and the effects of friction and temperature gradient can be accounted for in one iteration. As noted previously, this is not a definitive constitutive response for the ZrNb alloy, due to the assumed (fixed) temperature gradient in all tests. Greater accuracy would be expected if the evolution of the temperature gradient was measured and modelled, and incorporated in the FE analysis. This is the focus of current work on Ti alloys [42], which also addresses the question of applying the correction method for more sparse datasets (since a matrix of 9×8 test conditions is somewhat untypical).

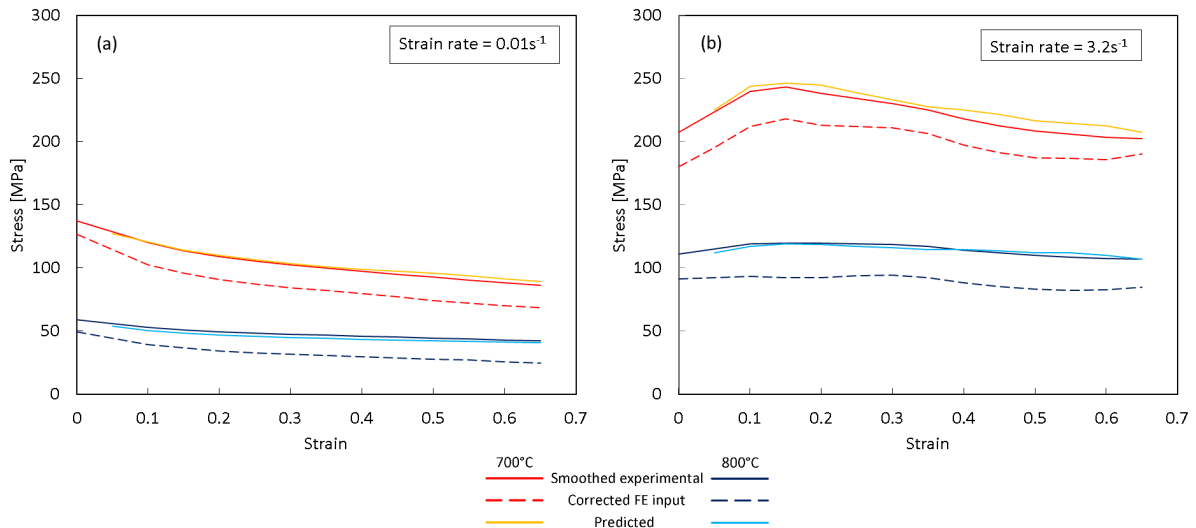


Figure 14 Experimental (smoothed) stress-strain curves, and FE predicted after correction of the input constitutive response, for the same nominal temperatures and strain-rates as Fig. 11.

7. Further applications of the FE model

The corrected constitutive data were used to generate a number of useful outputs from the FE model. Since the temperature distribution in the analysis is only estimated, the results should not be overinterpreted, but again serve as a proof of concept.

7.1 Mapping of deformation conditions

Figure 15 shows, for the end of the deformation ($\epsilon=0.69$), the (assumed) temperature field, and the predicted distribution of von Mises stress, equivalent plastic strain, and the axial and radial strain-rate components. Note the doubly-curved concave/convex form of the overall barrelling, seen experimentally in Fig. 3. The plastic strain distribution (Fig. 15b) shows the ‘dead metal zones’ adjacent to the workpiece-platen interfaces, and the resulting amplification of the strain in the centre of the sample. The distributions of strain-rate (Fig. 15d,e) also show the dead metal zones and magnified central axial strain-rate, and highlight the concentration of deformation into shear bands. Note that the maximum plastic strain and axial strain-rate at the centre are approximately 3–4 times the nominal values.

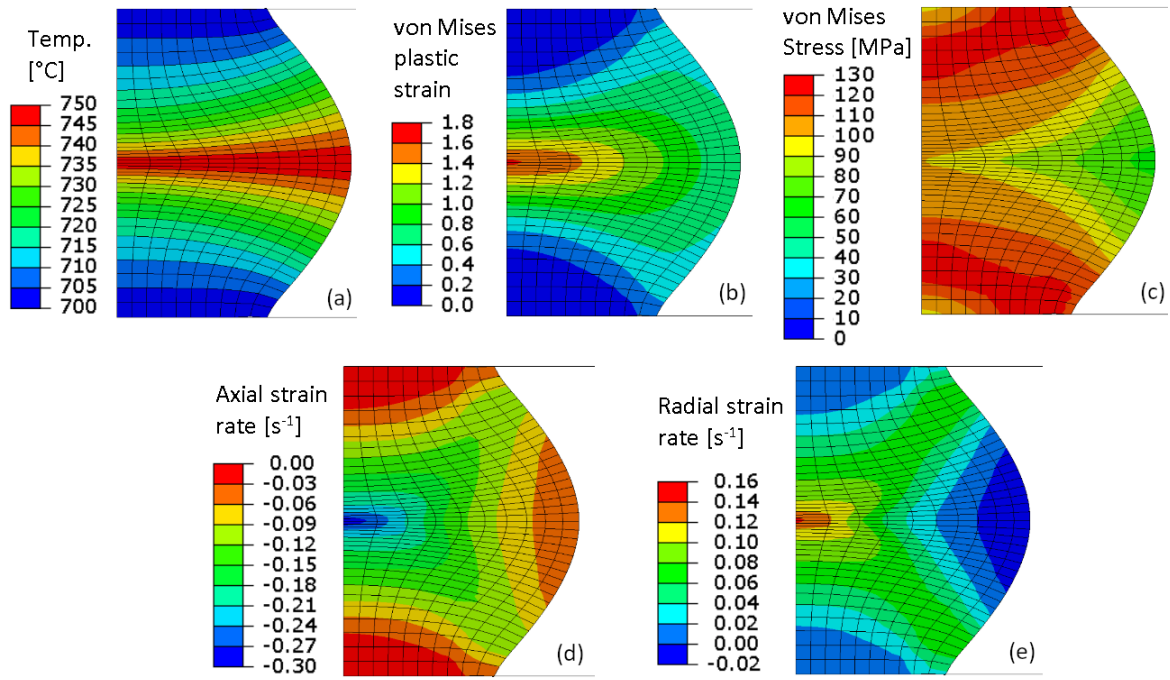


Figure 15 FE results obtained with smoothed, corrected stress-strain data at $T_{\text{nominal}} = 750^{\circ}\text{C}$, $\dot{\epsilon}_{\text{nominal}} = 0.1 \text{ s}^{-1}$, with $\mu=0.5$ and $\Delta T=50^{\circ}\text{C}$: (a) temperature; (b) equivalent plastic strain; (c) von Mises stress; (d) axial strain-rate; (e) radial strain-rate.

Another visualisation technique is proposed to indicate the spatial deviation of the local T and $\dot{\epsilon}$ conditions from the nominal value. Figure 16 shows a contour map of the von Mises equivalent plastic strain at the end of the test, as a function of the local temperature and strain-rate, for the proportion of the workpiece where significant strain occurs (above a lower limit of $\epsilon=0.2$). The peak contour value ($\epsilon=1.6$) indicates the maximum strain, and hence its magnification compared to the notional true value of 0.69, as well as the conditions at the point of maximum strain (here, a higher strain-rate at the nominal temperature, since the mid-plane temperature is assumed to be constant).

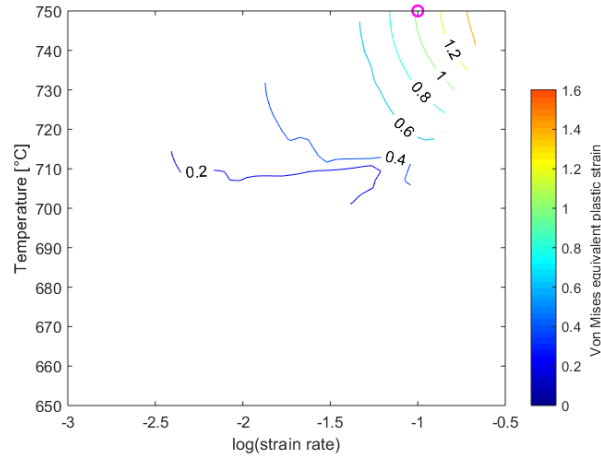


Figure 16 von Mises equivalent plastic strain as a function of temperature and strain-rate, for $T_{\text{nominal}} = 750^{\circ}\text{C}$, $\dot{\epsilon}_{\text{nominal}} = 0.1\text{s}^{-1}$ (indicated by the circle), with $\mu=0.5$ and $\Delta T = 50^{\circ}\text{C}$.

The history of the local deformation conditions at any point within the material cross-section may also be output from the FE model. Figure 17 shows the evolution of equivalent plastic strain, for the same conditions as Figs. 15-16, at the centre of the sample, and at a point on the mid-plane initially located at half the radius from the centre. Compared to the nominal test conditions, the strain-rate at both locations is immediately a factor of two greater at both locations, and remains at this level or above at the centre, while off-axis the strain-rate progressively falls. These differences are important in interpreting the evolution of microstructure throughout the sample, both in terms of average values and spatial variation – for example, texture pole figures are often evaluated over a significant proportion of the cross-section, in order to satisfy sampling statistics.

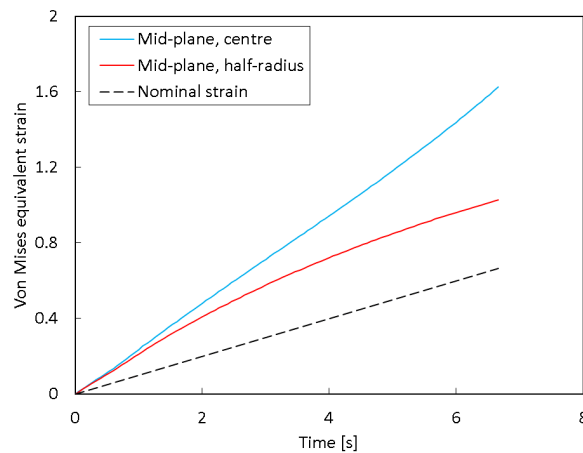


Figure 17 FE predicted evolution of von Mises equivalent plastic strain on the sample mid-plane, at the centre and at half the radius, for nominal $T = 750^{\circ}\text{C}$, $\dot{\epsilon} = 0.1\text{s}^{-1}$, with $\mu=0.5$ and $\Delta T = 50^{\circ}\text{C}$.

7.2 Prediction of extent of barrelling

A quantitative validation of the FE model is to compare the predicted shape of the deformed sample with experiment. Sample cross-sections, such as that shown in Fig. 3, show a degree of asymmetry (both top to bottom, and from one side to the other). The maximum area in every test was estimated with calipers (taking a geometric average of the local maximum and minimum diameters, in two perpendicular directions) [44]. Then by measuring the final length and assuming volume conservation, an average nominal final area was evaluated. The ratio of the measured maximum area to this nominal value gives a simple measure of barrelling. This was calculated for all 72 test conditions (averaging data for the duplicate tests). Figure 18 shows this ratio, as a statistically fitted contour map of $\log(\text{strain-rate})$ against temperature for the experimental data, with the equivalent map derived from the FE predictions. Both maps show a similar trend, barrelling increasing from top left of the map to bottom right, but the spread of values in the experiments is greater than predicted by the FE model – particularly the maximum ratio observed. There is considerable scatter and asymmetry in the experimental tests, leading to greater shape distortion, whereas the FE predictions remain perfectly axisymmetric. Refinement of the FE model to improve the fit with experiment is not justified, given the assumed temperature gradient, and the inherent microstructural variation.

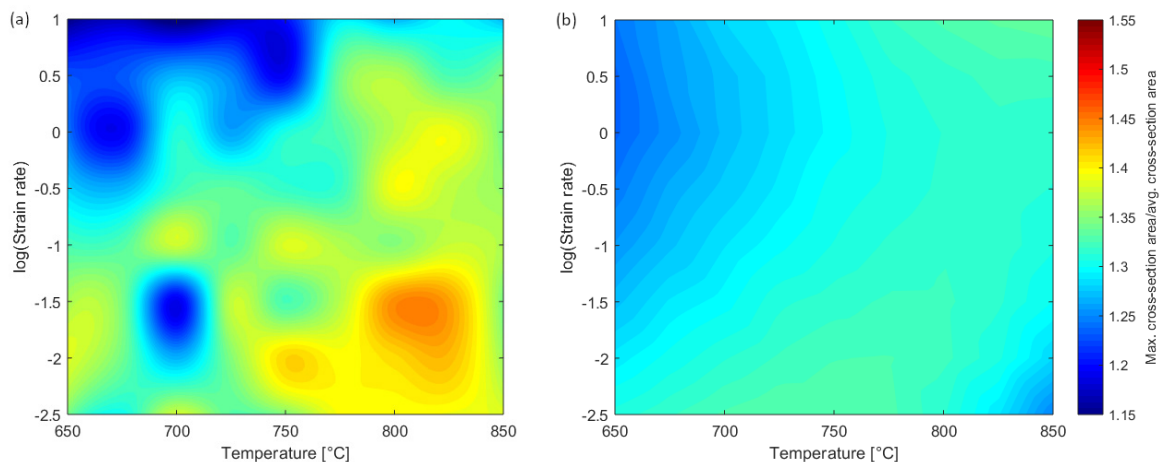


Figure 18 Ratio of the maximum cross-section area to the average cross-section area, as a function of temperature and $\log(\text{strain rate})$: (a) experimental data; (b) FE modelling results.

7.3 Prediction of strain-rate sensitivity

A parameter often investigated in hot deformation is the strain-rate sensitivity, $m = d(\log \sigma)/d(\log \dot{\epsilon})$. This parameter, plotted (at a reference strain) as a function of temperature and strain-rate, is commonly presented in the literature as a ‘processing map’. Strain-rate sensitivity is a parameter associated with the onset of flow instabilities, such as shear bands, flow localisation, and void formation, associated generally with inhomogeneous microstructures and poor performance. Processing maps are therefore regarded as a useful tool for identifying optimal conditions for controlling the target two-phase microstructure and texture development in the hot-working $\alpha + \beta$ regime [43] [48]. The approach has been criticised for lacking a robust physical basis, and for being incapable of accounting for complex deformation paths. Further issues are the variability of the results depending on the extent of the data and the different curve-fitting procedures used, demonstrated by Daniel et al. [43].

Here we illustrate the effect of using raw experimental true stress-strain data directly, without correction for inhomogeneous deformation in standard lab tests. Figure 19 shows a processing map for ZrNb derived from cubic fits to the raw experimental data (Fig 19a), and the equivalent plot using the FE corrected and smoothed constitutive data (Fig. 19b). The smoothed, corrected data gives a cleaner set of contours, and avoids significant noise and artefacts in the raw data (such as the negative rate-sensitivity at high strain-rates).

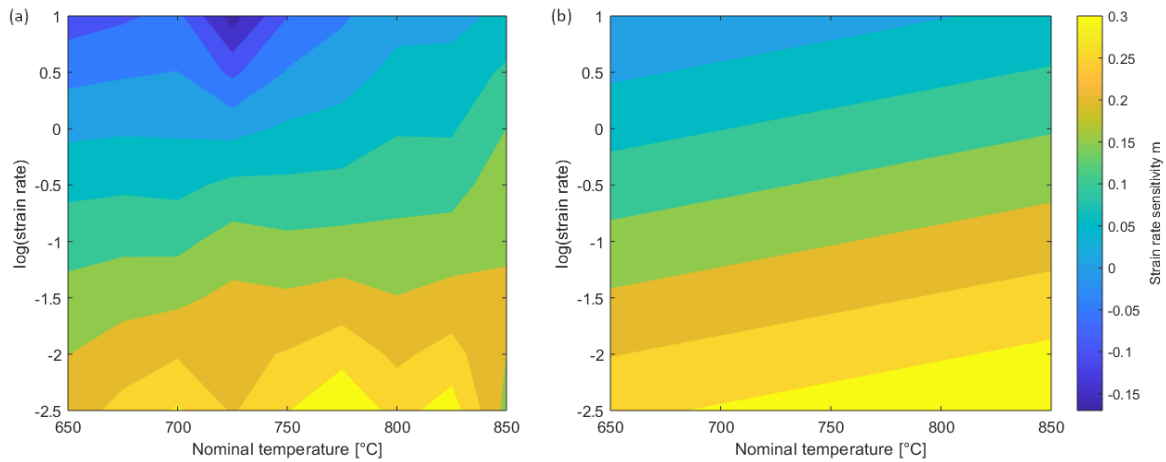


Figure 19 Processing maps of strain-rate sensitivity m , for ZrNb alloy, calculated from:

(a) cubic fit to the raw experimental data; (b) smoothed data corrected using the FE model;

8. Conclusions

A finite element model has been developed for a small-scale dilatometer rig used for hot compression testing of high temperature alloys, and applied to an extensive test series on ZrNb alloy. The FE analysis enabled the true stress-strain curves to be corrected in a single iteration, allowing for barrelling due to friction at the workpiece-platen interface, but also due to a temperature gradient between the mid-plane of the sample and the platen. In the current work, a fixed temperature gradient below the nominal test temperature was imposed, as a proof of concept.

The Sellars-Tegart (perfectly plastic) constitutive model was fitted with reasonable accuracy to the raw data at a low strain (5%), but the values found for physical parameters such as the activation energy were questionable, falling above the range expected from the literature. This model was however sufficient for setting up the FE model, and testing its sensitivity to boundary conditions and mesh size.

A novel approach was developed for fitting stress-strain data, discretising the strain rather than the temperature and strain-rate, and using quadratic surface fits for $\log \sigma = f(T, \log \dot{\epsilon})$, at discrete strains in intervals of 0.05. This smoothed the data efficiently, and provided robust extrapolation beyond the

domain of the experiments, notably down to zero strain-rate, which is required due to the dead metal zones in the sample.

A new methodology for correcting the flow stress data, due to inhomogeneity of the workpiece deformation, was implemented over the full matrix of test conditions. The smoothed low-order fit to the raw data was used as input to the FE model, and the resulting offset in flow stress was applied point-by-point to the original data, leading to a corrected function $\log \sigma = f(T, \log \dot{\epsilon})$ at discrete intervals in strain. The experimental notional stress-strain curves were predicted with good accuracy using the corrected constitutive response.

The FE model with the corrected data was applied to illustrate: (a) visualisation of the distribution and histories of local deformation conditions in the sample, relative to the nominal temperature and strain-rate (for use alongside interpretation of deformation microstructures); (b) broad correlation with experimental measurements of barrelling; and (c) prediction of strain-rate sensitivity, commonly presented as ‘processing maps’ in the literature.

Acknowledgements

This research was funded by *LightForm*, a UK Engineering and Physical Sciences Research Council (EPSRC) programme grant (EP/R001715/1). The authors wish to acknowledge the contribution of our *LightForm* colleagues: Dr Graham McShane at the University of Cambridge, and Dr. Chris Daniel, Prof. João Quinta da Fonseca, and Chris Peyton at the University of Manchester, for provision of the test data and for many technical discussions.

References

- [1] H.R. Shercliff, A.M. Lovatt, Philos. Trans. R. Soc. A 357 (1999) 1621-1643.
- [2] S.I. Oh, S.L. Semiatin, J.J. Jonas, Metall. Trans. A 23(3) (1992) 963–975.
- [3] G.E. Dieter, in: G.E. Dieter, H.A. Kuhn, S.L. Semiatin (Eds.), Handbook of Workability and Process Design, ASM International, Materials Park, Ohio, 2003, pp. 61-67.
- [4] T. Instruments, DIL 805A/D/T, <https://www.tainstruments.com/dil-805adt-quenching-dilatometers/>, 15 May 2020.

- [5] B. Roebuck, J.D. Lord, M. Brooks, M.S. Loveday, C.M. Sellars, R.W. Evans, *Mater. High Temp.* 23(2) (2006) 59-83.
- [6] Y.C. Lin, X.M. Chen, *Mater. Des.* 32(4) (2011) 1733–1759.
- [7] C. Zener, J.H. Hollomon, *J. Appl. Phys.* 15(22) (1944).
- [8] C.M. Sellars, W.J. McTegart, *Acta Metall.* 14(9) (1966) 1136-1138.
- [9] U.F. Kocks, A.S. Argon, M.F. Ashby, *Prog. Mater. Sci.* 19 (1975).
- [10] L. Briottet, J.J. Jonas, F. Montheillet, *Acta Mater.* 44(4) (1996) 1665-1672.
- [11] H.J. Frost, M.F. Ashby, *Deformation-mechanism maps: the plasticity and creep of metals and ceramics*, Pergamon Press, Oxford, 1982.
- [12] Y.C. Lin, M.S. Chen, J. Zhong, *Comput. Mater. Sci.* 42 (2008) 470-477.
- [13] Y.C. Lin, M.S. Chen, J. Zhong, *Mech. Res. Commun.* 35 (2008) 142-150.
- [14] G. Ji, F. Li, Q. Li, H. Li, Z. Li, *Mater. Sci. Eng. A* 528(13-14) (2011) 4774-4782.
- [15] Y.C. Lin, Y.C. Xia, X.M. Chen, M.S. Chen, *Comput. Mater. Sci.* 50(1) (2010) 227-233.
- [16] C. Liao, H. Wu, S. Lee, F. Zhu, H. Liu, C. Wu, *Mater. Sci. Eng. A* 565 (2013) 1-8.
- [17] P. Geng, G. Qin, J. Zhou, Z. Zou, *J. Manuf. Process.* 32 (2018) 469-481.
- [18] J. Cai, F. Li, T. Liu, B. Chen, M. He, *Mater. Des.* 32(3) (2011) 1144-1151.
- [19] Y. Hong, X. Cheng, G. Xiao, Y. Guo, *Mater. Sci. Eng. A* 528(21) (2011) 6510-6518.
- [20] S. Mandal, V. Rakesh, P.V. Sivaprasad, S. Venugopal, K.V. Kasiviswanathan, *Mater. Sci. Eng. A* 500(1-2) (2009) 114-121.
- [21] G. Ji, F. Li, Q. Li, H. Li, Z. Li, *Mater. Sci. Eng. A* 528 (2011) 4774–4782.
- [22] G.R. Johnson, W.H. Cook, in: *Proceedings of the 7th International Symposium on Ballistics*, The Hague, April 19-21, 1983, pp. 541-547
- [23] P. Jedrasiak, H.R. Shercliff, *Finite element modelling of small-scale hot deformation testing*, CUED Technical Report, CUED/C-MATS/TR264, Cambridge, December 2019.
- [24] K.M. Kulkarni, S. Kalpakjian, *J Eng. Ind.* 91(3) (1969) 743-754.
- [25] S.I. Oh, S.L. Semiatin, J. J. Jonas, *Metall. Trans. A* 23 (1992) 963–975.
- [26] J. Appa Rao, J. Babu Rao, S. Kamaluddin, M.M.M.Sarcar, N.R.M.R. Bhargava, *Mater. Des.* 30 (2009) 2143–2151.
- [27] B. Zhou, Y. Shen, J. Chen, Z. Cui, *J. Iron Steel Res. Int.* 18(1) (2011) 41-48.
- [28] J. Majta, J.G. Lenard, M. Pietrzyk, *Mater. Sci. Eng. A* 208 (1996) 249-259.
- [29] H. Monajati, A. K. Taheri, M. Jahazi, S. Yue, *Metall. Mater. Trans. A* 36 (2005) 895–905.
- [30] R. Ebrahimi, A. Najafizadeh, *J. Mater. Process. Technol.* 152 (2004) 136–143.
- [31] Y.P. Li, H. Matsumoto, A. Chiba, *Metall. Mater. Trans. A* 40A (2009) 1203-1209.
- [32] Y. Li, E. Onodera, A. Chiba, *Mater. Trans.* 51(7) (2010) 1210-1215.
- [33] Y.P. Li, E. Onodera, H. Matsumoto, A. Chiba, *Metall. Mater. Trans. A* 40 (2009) 982–990.
- [34] R.L. Goetz and S.L. Semiatin, *J. Mater. Eng. Perform.* 10(6) (2001) 710-717.
- [35] Y.P. Li, E. Onodera, H. Matsumoto, Y. Koizumi, S. Yu, A. Chiba, *ISIJ Int.* 51(5) (2011) 782-787.
- [36] M.C. Mataya, V.E. Sackschewsky, *Metall. Mater. Trans. A* 25A (1994) 2737-2752.
- [37] E. Parteder, R. Bunten, *J. Mater. Process. Technol.* 74 (1998) 227–233.
- [38] L. Xinbo, Z. Fubao, Z. Zhiliang, *J. Mater. Process. Technol.* 120(1-3) (2002) 144-150.
- [39] X. Wang, H. Li, K. Chandrashekhara, S.A. Rummel, S. Lekakh, D.C. Van Aken, *J. Mater. Process. Technol.* 243 (2017) 465–473.
- [40] H. Cho, G. Ngalle, T. Altan, *CIRP Ann.* 52(1) (2003) 221-224

- [41] D.J. Yu, D.S. Xu, H. Wang, Z.B. Zhao, G.Z. Wei, R. Yang, *J. Mater. Sci. Technol.* 35 (2019) 1039–1043
- [42] P. Jedrasiak, H.R. Shercliff, Modelling of thermal field and inhomogeneous deformation in hot compression of titanium alloys (unpublished work).
- [43] C.S. Daniel, P. Jedrasiak, C.J. Peyton, J.Q. da Fonseca, H.R. Shercliff, L. Bradley, P.D. Honniball in *19th International Symposium on Zirconium in the Nuclear Industry*, Manchester, May 20-23, 2019.
- [44] C. Peyton, Generating and evaluating the strain rate sensitivity processing maps for Zr-2.5Nb, Thesis, University of Manchester, 2018.
- [45] ASM Handbook volume 2: Properties and selection: Nonferrous alloys and special-purpose materials, 10th Ed., ASM International, Ohio, 1990.
- [46] F. Cardarelli, *Materials Handbook*, 2nd Ed., Springer-Verlag, London, 2008.
- [47] C. Herzig, U. Kohler, S.V. Divinski, *J. Appl. Phys.* 85(12) (1999) 8119-8130.
- [48] C.S. Daniel, An investigation into the texture development during hot-rolling of dual-phase zirconium alloys, Eng.D. Thesis, University of Manchester, 2018.